Lagrangian Flow Map Analysis of Ocean Dynamics and Material Transports

P.F.J. Lermusiaux[a,†], P.J. Haley, Jr.[a], C. Mirabito[a].
[a]*Department of Mechanical Engineering, Massachusetts Institute of Technology, Cambridge, MA*
[†]Corresponding author: pierrel@mit.edu

***Abstract*—In this paper, we illustrate the use of our partial differential equations for flow maps to quantify Lagrangian transports and non-advective dynamics in geophysical fluid flows. Our emphasis is on the use of spatiotemporal flow maps to help differentiate the advective transports from non-advective transformations of water masses and ocean features in four dimensions. Preliminary results are presented for real-time sea experiments with autonomous sensing platforms and advanced modeling systems in diverse ocean regions and dynamical regimes. They include the Nova Scotia Shelf-Slope and New England Seamount Chain regions, Gulf of Mexico, and Balearic and Alboran Seas in the western Mediterranean. Our differentiations directly highlight regions of higher shear and mixing, including the edges of meanders, eddies, filaments, and internal waves, and the regions undergoing strong vertical or spiral motions.**

***Index Terms*—Ocean modeling, dynamical systems, Lagrangian transports, flow map composition, coherent sets, Lagrangian Coherent Structures, incoherence, mixing**

I. Introduction

Ocean currents and atmospheric winds transport a variety of natural and man-made materials. Natural Lagrangian transports involve aerosols, pathogens, plankton, algae, sediments, and air and water masses themselves, while man-made quantities include pollutants, debris, floating objects, robots, or humans themselves in search and rescue operations. Due to advection and other forces such as Coriolis, buoyancy, tides, and boundary forcing, coherent structures such as fronts, jets, eddies, and gyres form. These coherent structures and their shear flows also lead to instabilities, turbulent stirring, and ultimately mixing through molecular diffusion. For both scientific understanding and practical applications, it is essential to predict, map, and characterize flow transports and flow structures across space and time. Equally useful is the ability to distinguish between advection, coherence, inertia, and reversible processes, and instabilities, incoherence, mixing, and irreversible processes.

Much progress has been made in understanding chaotic transports and coherent flow structures in fluid, ocean, and atmosphere dynamics [1–10]. Many transport studies first compute Lagrangian trajectories of passive water parcels. These trajectories, the corresponding flow maps, and their derivatives are then utilized to define and compute powerful quantities such as finite time Lyapunov exponents (FTLEs) and other common types of Lagrangian Coherent Structures (LCSs) [11–15]. The results originating from flow maps and dynamical system analyses include attracting basins, repulsive surfaces, residence times, connectivity patterns, and coherent and incoherent sets. In fluid dynamical systems, a classic flow map indicates where each parcel of water is transported after a given time, forward or backward. For a finite-time trajectory, the forward flow map is the function that maps the initial location to the final location, while the backward flow map maps the final location back to the initial location. In other words, the forward flow map field is the final destination at each start location, while the backward flow map field is the start location at each final destination.

In this work, we highlight and extend the use of our partial differential equation (PDE) methods for flow map and Lagrangian transport studies in geophysical fluid flows [16–20]. They include super-accurate schemes for advective transport through flow map composition, achieving minimal errors and strong theoretical guarantees. Flow maps are spatiotemporal fields governed by PDEs that correspond to an infinite number of classic trajectories governed by ODEs (the characteristics of the PDEs). We can utilize our four-dimensional flow map predictions to extract dynamical regions and classify ocean processes, and inform classical geophysical fluid dynamics analyses [21–24]. An emphasis of the present exploration is to highlight the use of PDE-based flow maps to help differentiate the advective transports from non-advective transformations of water masses and ocean features in four dimensions. Preliminary results are presented for real-time at-sea experiments with autonomous sensing platforms in diverse ocean regions and dynamical regimes. They include the northwestern Atlantic, Gulf of Mexico, and western Mediterranean.

The spatiotemporal ocean fields that we employ are real-time forecasts or reanalyses from our MIT-MSEAS data-assimilative Primitive-Equation (PE) submesoscale-to-regional-scale ocean-modeling system [25–27]. These multi-resolution simulations were forced with tides and air-sea fluxes and initialized by downscaling from global models. Flow maps and derived Lagrangian quantities are then obtained using the MIT-MSEAS velocity fields.

In what follows, we outline our Lagrangian flow map methods and ocean modeling systems. We then showcase transports and transformations of water masses in the Nova Scotia Shelf-Slope and New England Seamount Chain region, multiscale stirring and mixing in Gulf of Mexico, subduction pathways in the Balearic Sea, and dynamical flow structures in the Alboran Sea. We then provide brief conclusions.

II. Methodology

Our Lagrangian approach consists of computing flow maps [16, 18, 28, 29] using super-accurate schemes to integrate advection PDEs for Lagrangian transport of positions and field variables of interest. We then characterize these transports, compute flow structures, and differentiate pure advection processes from complete dynamical processes. The flow velocity

Authorized licensed use limited to: MIT. Downloaded on December 03,2025 at 16:46:51 UTC from IEEE Xplore. Restrictions apply.

979-8-218-73628-6 ©2025 MTS

fields used in the advection are the ocean currents predicted by our data-assimilative ocean modeling.

A. Lagrangian Flow Map

To compute flow maps, we employ our PDE-based method of composition [17] extended for use in realistic open-flow fields, with time-dependent inlets and outlets [19].

The advective transport of a generic (possibly vector valued) quantity α defined per unit mass is governed by Eq. (1), over some open spatial domain Ω, with inlets and outlets,

$$\begin{aligned} &\frac{\partial \alpha(\boldsymbol{x},t)}{\partial t} + \boldsymbol{v}(\boldsymbol{x},t)\cdot\nabla\alpha(\boldsymbol{x},t) = 0\,, \\ &\alpha(\boldsymbol{x},0) = \alpha_0\,, \end{aligned} \tag{1}$$

where $\boldsymbol{v}$ is the velocity field and $\alpha(\boldsymbol{x},0) = \alpha_0(\boldsymbol{x})$ the initial condition (IC). This PDE governs the motion of fluid parcels initially in position $\boldsymbol{x}_0$, carrying the quantity $\alpha_0(\boldsymbol{x}_0)$, and advected by the velocity field $\boldsymbol{v}(\boldsymbol{x}(t),t)$. By definition, the position of this parcel at the final time T (denoted by $\boldsymbol{x}$) is given by the forward flow map $\boldsymbol{x} = \boldsymbol{\phi}_0^T(\boldsymbol{x}_0)$. The backward flow map is the inverse of the forward flow map. Hence, we can also write the advection relation in terms of the backward flow map as $\boldsymbol{x}_0 = \left(\boldsymbol{\phi}_0^T\right)^{-1}(\boldsymbol{x}) = \boldsymbol{\phi}_T^0(\boldsymbol{x})$.

For the quantity α governed by Eq. (1), we thus have

$$\alpha(\boldsymbol{x},T) = \alpha_0(\boldsymbol{x}_0) = \alpha_0(\boldsymbol{\phi}_T^0(\boldsymbol{x})) \quad \forall\ \boldsymbol{x}\in\Omega_a(T)\,,$$

where $\Omega_a(t)$ is the active domain or the region of Ω where the flow map is defined [19]. If we now consider for α the 3D field of parcel positions, for the IC $\alpha_0(\boldsymbol{x}) = \boldsymbol{x} \quad \forall\ \boldsymbol{x}\in\Omega$, we then have that:

$$\alpha(\boldsymbol{x},T) = \alpha_0(\boldsymbol{x}_0) = \boldsymbol{\phi}_T^0(\boldsymbol{x}) \quad \forall\ \boldsymbol{x}\in\Omega_a(T)\,. \tag{2}$$

The backward flow map $\boldsymbol{\phi}_T^0(\boldsymbol{x})$ is thus governed by the following PDE system forward in time with the given IC [19],

$$\begin{aligned} &\frac{\partial \alpha(\boldsymbol{x},t)}{\partial t} + \boldsymbol{v}(\boldsymbol{x},t)\cdot\nabla\alpha(\boldsymbol{x},t) = 0\,, \\ &\alpha(\boldsymbol{x},0) = \boldsymbol{x}\,, \\ &\text{then}\quad \alpha(\boldsymbol{x},T) = \boldsymbol{\phi}_T^0(\boldsymbol{x})\,. \end{aligned} \tag{3}$$

Similarly, the forward flow map $\boldsymbol{\phi}_0^T(\boldsymbol{x})$ can be obtained by solving the following PDE system backward in time, with the stated terminal condition:

$$\begin{aligned} &\frac{\partial \alpha(\boldsymbol{x},t)}{\partial t} + \boldsymbol{v}(\boldsymbol{x},t)\cdot\nabla\alpha(\boldsymbol{x},t) = 0\,, \\ &\alpha(\boldsymbol{x},T) = \boldsymbol{x}\,, \\ &\text{then}\ \alpha(\boldsymbol{x},0) = \boldsymbol{\phi}_0^T(\boldsymbol{x})\,. \end{aligned} \tag{4}$$

These PDE flow map systems are simply what we solve for advection-only dynamics. Using appropriate boundary conditions, Eq. (3) and Eq. (4) are numerically integrated using the efficient and super-accurate method of composition [17, 19].

B. Ocean Modeling Systems

The ocean fields we employ were simulated using our probabilistic MSEAS modeling system [25, 26, 30]. MSEAS has been used for scientific simulations and research forecasts in many ocean regions [e.g., 22, 27, 31–53]. In our applications, we employ its hydrostatic primitive-equation (PE) model with second-order structured finite volumes, generalized-level vertical coordinates, a nonlinear free surface, and implicit two-way nesting/tiling for multiscale dynamics [25, 26]. We also utilize our schemes for initialization and fast-marching objective analysis [26, 54], nested tidal prediction and inversion [55], subgrid-scale models [56, 57]. and ensemble forecasting and data assimilation with Error Subspace Statistical Estimation (ESSE) [58–61]. Other applications of MSEAS include underwater acoustics [33, 35, 53, 62–66], biogeochemical-ecosystem simulations and learning [38, 67–70], ocean monitoring and environmental assessment [21, 71–75], rapid responses [76, 77], reduced-order modeling onboard ocean vehicles [78–80], reachability analysis and path planning [42, 81–90], and adaptive sampling [43, 52, 61, 91–94].

III. Applications

We now illustrate the use of our PDE-based flow maps, advective transports, non-advective transformations, and coherent structures in four regions: the Northwest Atlantic Ocean, the Gulf of Mexico, the Balearic Sea, and the Alboran Sea.

A. Water Mass Transports and Transformations in the Northwest Atlantic Ocean

We first highlight the transport and transformation of water masses in the Nova Scotia Shelf-Slope and New England Seamount Chain region (Fig. 1). The ocean fields we used as input for this study are forecasts issued during the Intensive Observation Period (IOP) of the collaborative New England Seamount Acoustic (NESMA) sea experiment in the New England Seamount Chain in July 2024 [95]. These MSEAS ocean forecasts were commonly 3 to 5 days in duration, using 100 optimized vertical levels and 2.4 km horizontal resolution. Initial conditions were downscaled from two global models (HYCOM and Mercator) and corrected using some

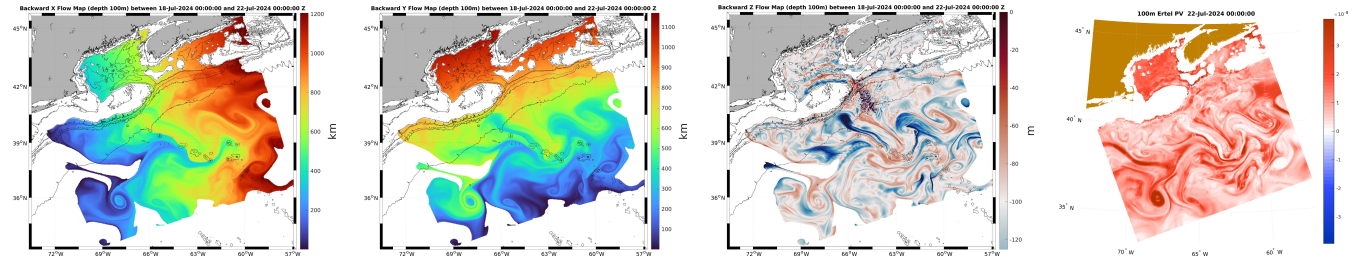

(a) 4-day bkwd. x flow map at 100 m (b) 4-day bkwd. y flow map at 100 m (c) 4-day bkwd. z flow map at 100 m (d) July 22 Ertel potential vorticity

Fig. 1: Water transports in the northwest Atlantic during July 18–22, 2024. (a,b) 4-day backward x and y flow maps at 100 m reveal the origins and extent of filaments off the shelf. (c) 4-day backward z flow map at 100 m reveals locations of parcels that have upwelled (blue) and downwelled (red) to 100 m after 4 days. (d) Ertel potential vorticity on July 22, has high correlation with the backward flow maps.

Authorized licensed use limited to: MIT. Downloaded on December 03,2025 at 16:46:51 UTC from IEEE Xplore. Restrictions apply.

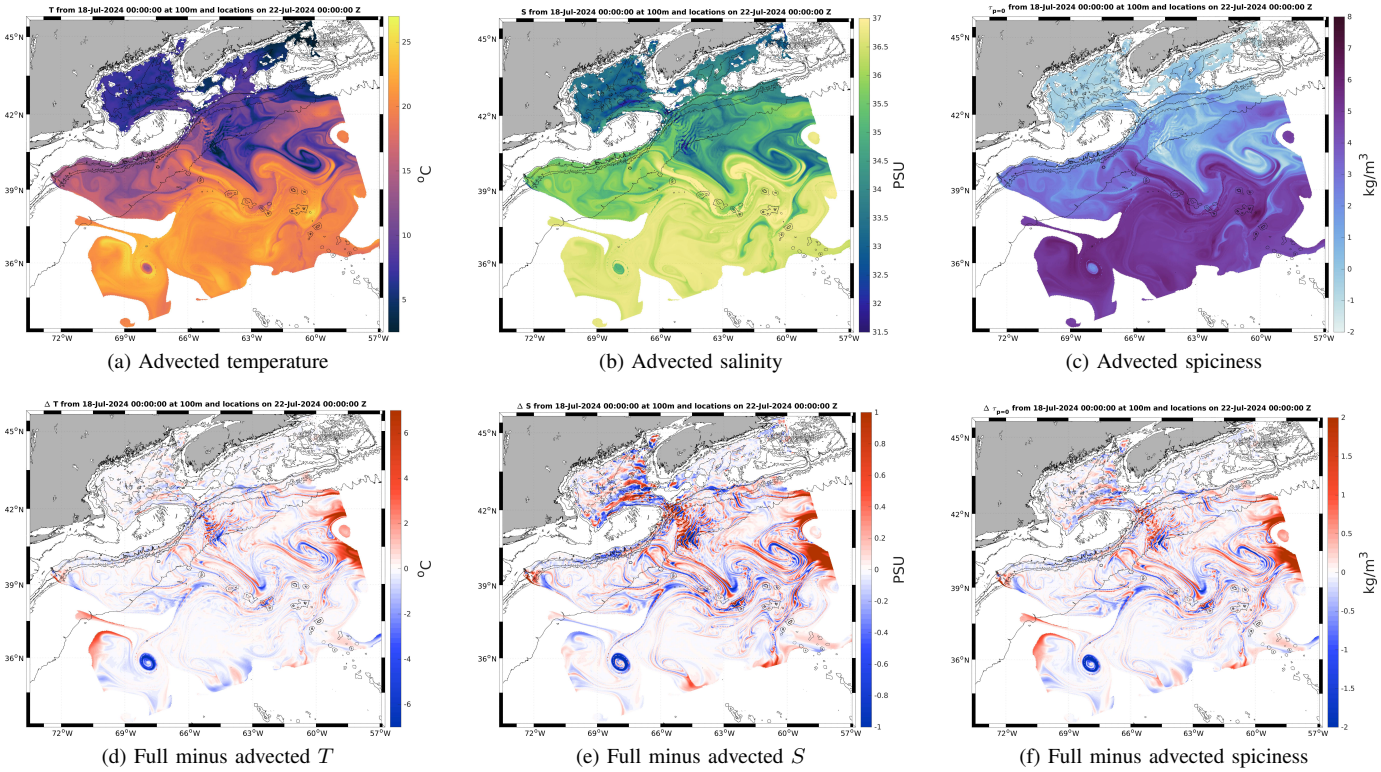

(a) Advected temperature (b) Advected salinity (c) Advected spiciness

(d) Full minus advected T (e) Full minus advected S (f) Full minus advected spiciness

Fig. 2: Water transports and mixing in the northwest Atlantic during July 18–22, 2024. Top row: Initial (a) temperature, (b) salinity, and (c) spiciness of water parcels purely advected by backward flow maps to 100 m depth after 4 days. Bottom row: Differences between full MSEAS-PE fields and purely advected fields, for (d) temperature, (e) salinity, and (f) spiciness, display how non-advective processes change the water mass properties.

data of opportunity. They were forced by blended atmospheric flux field forecasts from the High-Resolution Window (HIRESW) 5 km Model and Global Forecast System (GFS) 0.25° model from the National Centers for Environmental Prediction (NCEP), and by tides from TPXO9-Atlas of OSU adapted to the higher-resolution bathymetry and coastlines [55]. We utilized a bathymetry blended from the Shuttle Radar Topography Mission (SRTM) 15-arcsecond global map [96] and the 1-arcsecond NOAA coastal relief bathymetry [97]. Ocean physics and acoustics forecasts were issued daily.

In Figs. 1 and 2, we exemplify the direct use of flow maps for analyzing Lagrangian transports and the actual degree of conservation of dynamical tracers such as temperature T, salinity S, and spiciness during these transports. Spiciness is related to density-compensated variations in potential T and S. It is a variable whose isopycnal variations reflect isopycnal water-mass contrasts in density units [98].

Fig. 1 first predicts the 3D origin, extent, and potential vorticity properties of streamers and filaments of Nova Scotia shelf water being entrained off the shelf in the northwestern Atlantic Ocean during July 18–22, 2024. It also highlights known properties of features in this region, including those of Gulf Stream meanders, cold eddies (CEs), and warm core rings (WCRs) [99, 100]. Backward flow maps are thus used (Fig. 1a-c): they show the initial locations of fluid parcels at their final positions, hence the origin of water parcels and features. As a reminder, a single x, y, or z backward flow map over a specified time window, at a specified depth, does not by itself describe the full 3D movement of water parcels: it merely shows the x, y, or z origin of all water parcels that end up at the specified depth at the end of the time window. For example, Fig. 1a only shows the initial x coordinates of all parcels that end at 100 m after 4 days, and does not indicate the initial latitude or depth. The backward flow maps of horizontal positions shown in Fig. 1a and 1b reveal the origins of filaments off the shelf and alongside the Gulf Stream, while the backward flow map of vertical position (Fig. 1c) reveals the locations of parcels that upwelled (blue) or downwelled (red) to 100 m after 4 days. Synthesizing Figs. 1a–c provides a fuller picture of the 3D motions: we find that during July 2024, filaments originated from the western flank of Browns Bank, likely spillovers off the Nova Scotia shelf (Fig. 1a–b), at around 80 m depth (Fig. 1c), and were advected southeast, parallel to the New England seamount chain, to reach 100 m depth (downwelling). The Gulf Stream (GS) enters the domain near (39°N, 72°W); the white coloring in this area indicates parcels originated outside the PE ocean domain (flow maps are computed in what we call the active domain $\Omega_a(t)$). The GS interactions with the near-shelf fields and jets likely also contributed to this offshore entrainment. Immediately to the southwest of these Nova Scotia waters, a return branch upwells waters towards Georges Bank. Additional filaments can be seen east (downstream) of the Seamounts, e.g., near (39°N, 60°W), as well as remnants of WCRs. Lastly, the Ertel potential vorticity (PV) forecast at the end of the 4 days, on July 22, is shown on Fig. 1d. The high correlation between

Authorized licensed use limited to: MIT. Downloaded on December 03,2025 at 16:46:51 UTC from IEEE Xplore. Restrictions apply.

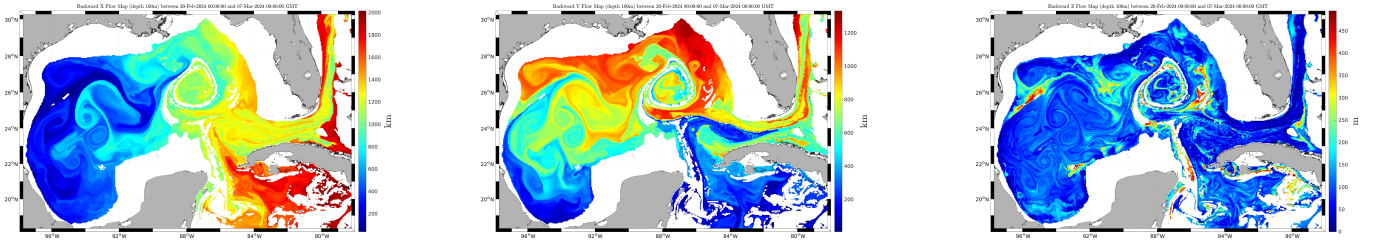

(a) 16-day bkwd. x flow map at 100 m (b) 16-day bkwd. y flow map at 100 m (c) 16-day bkwd. z flow map at 100 m ($z > 0$)

Fig. 3: Water mass transports in the Gulf of Mexico during February 20–March 7, 2024.

the Ertel PV and the backward x and y flow maps show that it is largely conserved in the Lagrangian sense along the filaments and most water motions. It is around zero mostly on the southern, inshore-bound (northwestward), and upwelling branch of the filamentation system. We also note in Fig. 1a,b the spiralling CE near (36°N, 68°W) that remained a long time in the region is estimated to have a high Ertel PV,

Fig. 2 examines the transport of watermass properties and their possible transformation and mixing during this transport, focusing on temperature, salinity, and spiciness. In the top row (Fig. 2a–c), the initial temperature, salinity, and spiciness are mapped to their final positions using the 4-day backward flow maps. These images represent what these fields would be if they had experienced advection only during these 4 days. In the bottom row (Fig. 2d–f), the fields of the top row are subtracted from the full PE simulation values for temperature, salinity, and spiciness. These differences highlight the regions where the non-advective processes modify the watermass properties. The sign convention is that a positive/negative difference indicates an increase/decrease in the water mass property by the non-advective processes. The main differences are largely along the edges of streamers/filaments, CEs and WCRs (39° to 42°N, 58° to 59°W). Significant differences also occur by topography. Mixing due to internal tides is also forecast in the Gulf of Maine, the Northeast Channel fan, and in the Hudson Canyon. Finally, we predict that non-advective processes associated with streamers/filaments and internal tides tend to produce alternating bands of increasing/decreasing watermass properties while those associated with CEs and WCRs seem to produce monolithic blocks of increasing or decreasing watermass properties.

B. Multiscale Stirring and Mixing in the Gulf of Mexico

We now showcase four-dimensional Lagrangian transports and multiscale stirring and mixing in the Gulf of Mexico. In this example, the ocean fields we used as input for the flow map PDEs are forecasts issued during the collaborative Mini-Adaptive Sampling Test Run (MASTR) ocean experiment in February–April 2024 [52, 101]. Forecasts were of 5 to 14 days in duration using 100 optimized vertical levels and 1/25° horizontal resolution. Initial conditions were downscaled from HYCOM and Mercator, and forced by blended NAM 12 km and GFS 0.25° hourly air-sea fluxes from NCEP and by tides from TPXO8-Atlas. We utilized the bathymetry from the Shuttle Radar Topography Mission (SRTM) 15-arcsecond global map [96], merged with the CICESE bathymetry for the Cozumel region. Forecast fields were issued daily.

In Figs. 3 and 4, we showcase the direct use of flow maps for analyzing Lagrangian transports and the degree of conservation of temperature, salinity, and potential density during these 3D transports.

Fig. 3 shows forecasts of backward flow maps of horizontal and vertical positions for February 20 to March 7, 2024. The colored flow map fields represent all the water parcels that start and remain in the 3D domain above 500 m depth and end up at 100 m depth after 16 days on March 7. Fig. 3a–b show that Caribbean waters are advected northward through the Yucatan Strait while the Loop Current (LC) and Gulf waters are advected eastward out of the Florida Strait and northward east of Florida. In these transports that all end up at 100 m, the western waters of the Caribbean Current mostly upwell through the Yucatan Strait and along Campache Bank while the LC waters mostly downwell through the Florida Strait (Fig. 3c). Our real-time forecast of the new LC eddy (LCE) Cardone shows turbulent spiralling of waters of different origins (Figs. 3a,b) and complex upwelling motions (Fig. 3c). Streamers of western Gulf water are advected north of Cardone, while streamers off the Florida escarpment are advected westward south of Cardone. Broad upwelling also occurs within streamers of western Gulf waters.

We also illustrate the use of 3D flow maps to differentiate advection from mixing and other non-advective processes. For example, Fig. 4 explores the evolution of water masses in LCE Cardone by showing how non-advection processes change the temperature, salinity, and potential density fields in time and space. In the top row (Fig. 4a-c), the initial temperature, salinity, and potential density are simply advected in a fully conservative fashion, using the 16-day backward flow maps. This pure advection computation is immediate as a simple mapping (e.g., $\alpha(\boldsymbol{x}, T) = \alpha_0(\boldsymbol{\phi}_T^0(\boldsymbol{x}))$; see Sec. II). In the bottom row (Fig. 4d-f), the pure flow map advection fields of the top row are subtracted from the full PE simulation values for temperature, salinity, and potential density. Our predictions show that non-advective processes tend to decrease temperature (increase density) in the LC south of Cardone and along topography (Fig. 4d,f). However, mixing and other non-advective processes tend to increase temperature (decrease density) in Cardone and in the streams of western Gulf waters (Fig. 4d,f). Non-advective processes also tend to increase salinity in the LC south of Cardone, around the outer edges of Cardone, and in the streams of western Gulf waters (Fig. 4e). Interestingly, they also decrease the salinity in the core of Cardone. Finally, we note that potential density has non-

Authorized licensed use limited to: MIT. Downloaded on December 03,2025 at 16:46:51 UTC from IEEE Xplore. Restrictions apply.

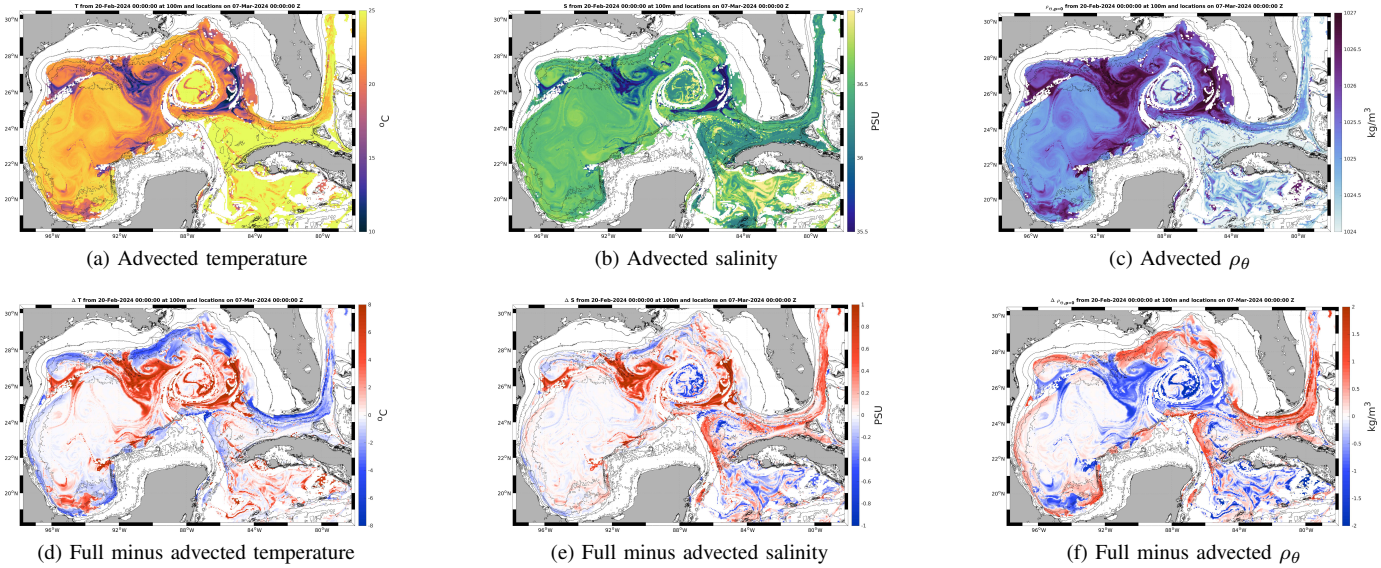

(a) Advected temperature (b) Advected salinity (c) Advected ρ_θ

(d) Full minus advected temperature (e) Full minus advected salinity (f) Full minus advected ρ_θ

Fig. 4: Water transports and mixing in the Gulf of Mexico during February 20–March 7, 2024. Top row: initial (a) temperature, (b) salinity, and (c) potential density of water parcels purely advected by backward flow maps to 100 m depth after 16 days. Bottom row: Differences between full MSEAS-PE fields and purely advected fields, for (d) temperature, (e) salinity, and (f) potential density, display how non-advective processes change the water mass properties.

advective patterns very similar to temperature in the GoM and east of Florida, but similar to salinity in the Carribean.

C. Subduction Regions and Transport Pathways in the Balearic Sea

We now turn to subduction studies conducted in the Balearic Sea; in this case, the ocean fields used as input are forecasts issued during the two-part CALYPSO Balearic Sea experiment in February–June 2022 [24, 102]. These implicit 2-way nested forecasts had horizontal resolutions of 900 m and 300 m with 70 optimized vertical levels. The ICs were downscaled from $1/50°$ WMOP [103, 104], updated based on available CALPYSO and Argo data, and forced with GFS air-sea fluxes and TPXO8-Atlas. We used the SRTM15 bathymetry.

Fig. 5 illustrates our MSEAS real-time flow map forecast products for the Balearic Sea using our interactive Seavizkit visualization [105, 106] as well as our FTLE and dilation forecast products. All products are forecasts for the 4-day time window from February 28–March 4, 2022. In the top row (Fig. 5a–d), we illustrate surface features. The 4-day forward x, y, and z flow maps at 3 m (Fig. 5a–c) forecast where fluid parcels initially at 3 m go as they are advected over 4 days. These forward flow maps reveal a jet that advects to the northeast along the northern Spanish coast and a second jet that circles Majorca and Minorca going northeast and then east (protrusions of red in x flow map, and blue in y flow map). Along the southern Spanish coast the flow maps highlight a southward jet (protrusion of blue x flow map). Of particular importance for the CALYPSO DRI, the blue areas of the forward z flow map show the initial positions of fluid parcels initially at 3 m that were forecast to be later subducted over the 4-day window. Fig. 5d is a dilation map forecast at 0 m computed using the 4-day flow maps. The dilation rate [107] measures the change in the area of an infinitesimal fluid patch over a finite time. It is also the average divergence experienced by a fluid parcel along its trajectory and is often used to find regions of accumulation at the surface and regions with larger vertical excursions [50, 107, 108]. We see a high correlation between the forecast dilation map (Fig. 5d) and downwelling directly predicted from the 4-day forward z flow map (Fig. 5c). In the bottom row (Fig. 5e–g), the 4-day backward x, y, and z flow map forecasts at 102 m show where parcels came from as they were advected over 4 days. Off southern Spanish shelf, the 4-day backward flow maps reveal a deep northward flowing jet (blue protrusion in backward x flow map). In the northern Balearic Sea, several southward flowing filaments can be seen in the 4-day backward flow maps (red protrusions in backward x flow map). Several streamers are also forecast to come off the Spanish shelf (red protrusions in backward y flow map). Focusing on subduction, we note that the red regions of the backward z flow map show the final locations of parcels forecast to downwell to 100 m over 4 days. We see a complex submesoscale mixture of upwelling/downwelling fronts, jets, and eddies, in the northern Balearic Sea. Fig. 5h shows our forward FTLE forecast computed from 4-day flow maps and highlights the repelling separatrices in the flow field. We see a high correlation between the structures in the backward flow maps (Fig. 5e–g) and the separatrices of the FTLE (Fig. 5h).

D. Dynamical Flow Structures in the Alboran Sea

Finally, we explore structures of flow fields themselves in the western Mediterranean Sea using dynamical system analysis tools that we compute from flow maps. For this analysis, the ocean fields used as input are forecasts we issued during the CALYPSO Alboran Sea experiment in March–April 2019 [23, 49, 109, 110]. These MSEAS forecasts had a $1/200°$ resolution with 70 optimized vertical levels, initialized from one of HYCOM, CMEMS, or WMOP, downscaled and data-

Authorized licensed use limited to: MIT. Downloaded on December 03,2025 at 16:46:51 UTC from IEEE Xplore. Restrictions apply.

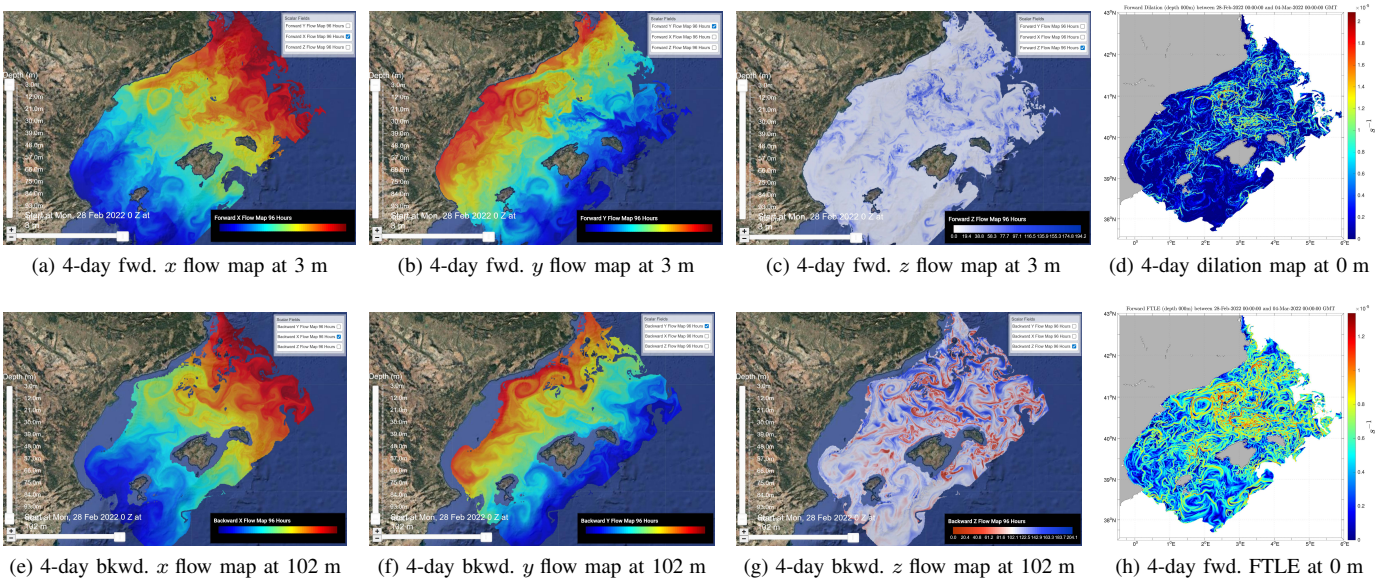

(a) 4-day fwd. x flow map at 3 m (b) 4-day fwd. y flow map at 3 m (c) 4-day fwd. z flow map at 3 m (d) 4-day dilation map at 0 m

(e) 4-day bkwd. x flow map at 102 m (f) 4-day bkwd. y flow map at 102 m (g) 4-day bkwd. z flow map at 102 m (h) 4-day fwd. FTLE at 0 m

Fig. 5: Water mass transports and subduction in the Balearic Sea: MSEAS flow map, dilation, and FTLE forecast products during February 28–March 4, 2022 (4-day duration). Top Row: 3 m forward (a) x, (b) y, and (c) z flow maps. (d) Dilation map at 0 m. Bottom Row: 100 m backward (e) x, (f) y, and (g) z flow maps. (h) Forward FTLE map at 0 m and its repelling separatrices.

corrected. The tidal and atmospheric forcing and bathymetry were the same as those for the Balearic Sea experiment.

Fig. 6 displays MSEAS flow maps, FTLEs, and vorticity forecasts for the Alboran Sea. Figs. 6a–b show the 4-day forward x and y flow maps for April 10–14, 2019 at 4 m. Figs. 6c,f show flow diagnostic fields computed from flow maps: specifically the 4-day forward and backward FTLEs that show repelling and attracting regions. Figs. 6d,e show the 2 m scaled-vorticity snapshots at 12Z on April 12 (mid-point of flow map and FTLE computations) and 14 (end of flow map and FTLE computations). Using the flow maps to dissect the Alboran flow field, its sharp features are striking, indicating that waters of very different destinations are initially very close to each other. This is confirmed by the repulsive ridges of the forward FTLE and sharp positive vorticity streams. The most striking ridges are the bifurcated coastal currents along the Spanish coast south of Almería at 2°W (the creation of the Almería–Oran front) and south of Málaga at 4°W. For example, the x flow map reveals at 4°W that the western portion flows west while the eastern portion flows east. These x and y flow maps also indicate that the Western Alboran Gyre (WAG) makes about a half-turn over the 4 days of flow map calculation. The southern half of the eastern Alboran Sea (after the Alboran ridge) has large eastward flows, especially near the African coast. The northern half shows an anticyclone (see vorticity fields) around 36.5°N between 1°W and 2°W. The x and y flow maps in this region are consistent with the anticyclone (the southern portion moves east and north while the northern portion moves west and south). We also note that fluid parcels along the northern edge of the anticyclone are advected out of the domain to the east (shown by unfilled breaks in the x and y flow maps). Figs. 6a–c reveal a high correlation between the repelling separatrices of the forward FTLE and the x and y flow maps. Similarly, Figs. 6d–f show a high correlation between the attracting separatrices of the backward FTLE map and the vorticity fields. These again highlight that dynamical systems' quantities such as FTLEs agree with and complement classic ocean dynamics descriptors.

IV. Conclusions

In conclusion, our studies confirm that flow maps and their derivatives are important tools to predict, map, and characterize transports and flow structures across space and time. Our preliminary results also highlight that flow maps and their derivatives, when advective transport is differentiated from full ocean dynamics, can be equally useful in distinguishing advection, coherence, inertia, and reversible processes from instabilities, incoherence, mixing, and irreversible processes. In the future, for such differentiations, we can employ objective criteria that predict and classify sets of fluid parcels that remain most coherent/incoherent, stirred/mixed, or reversible/irreversible throughout an extended time interval. There are diverse theoretical and applied opportunities.

Acknowledgments

We thank all members of our MSEAS group for useful discussions. We thank all members of the New England Seamount Acoustic (NESMA) team, Understanding Gulf Ocean Systems (UGOS) Initiative, and Coherent Lagrangian Pathways from the Surface Ocean to Interior (CALYPSO) Departmental Research Initiative. We thank the HYCOM Consortium and Mercator Ocean for their ocean model fields, and NCEP for their atmospheric forcing forecasts. We are grateful to the Office of Naval Research for support under Grants N00014-19-1-2664 (Task Force Ocean: DEEP-AI), N0014-18-1-2781 (CALYPSO–4D-LANES), and N00014-24-1-2715 (DRI-RIOT) to the Massachusetts Institute of Technology (MIT). We also acknowledge support from the Gulf Research

Authorized licensed use limited to: MIT. Downloaded on December 03,2025 at 16:46:51 UTC from IEEE Xplore. Restrictions apply.

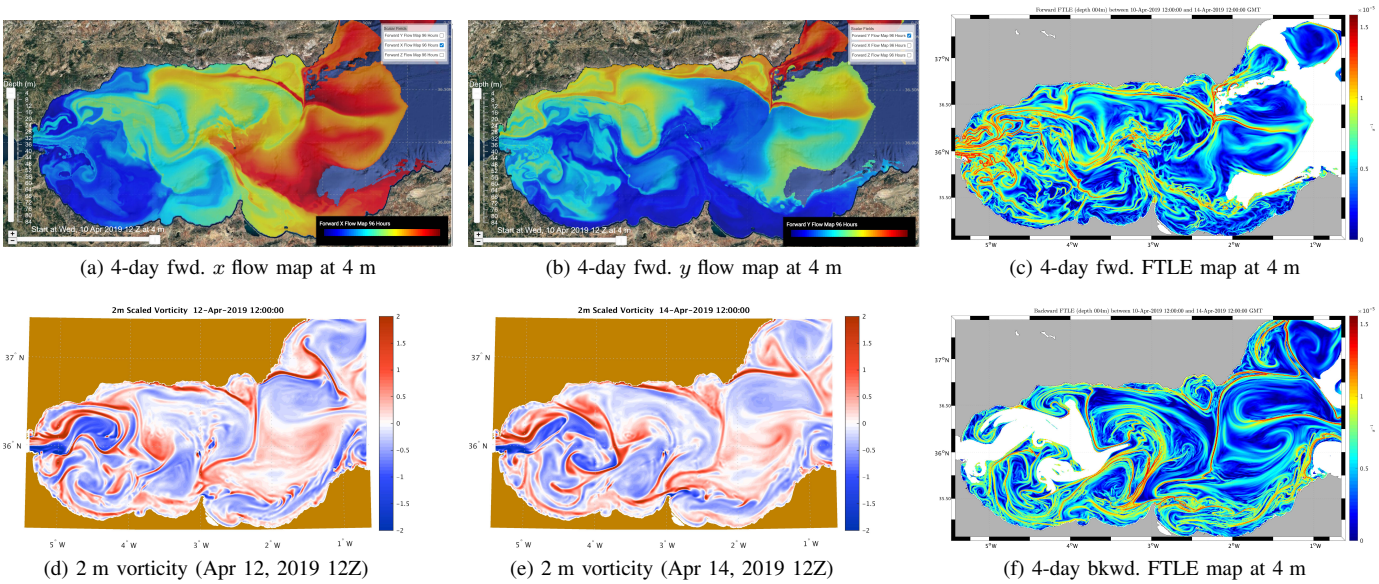

(a) 4-day fwd. x flow map at 4 m (b) 4-day fwd. y flow map at 4 m (c) 4-day fwd. FTLE map at 4 m

(d) 2 m vorticity (Apr 12, 2019 12Z) (e) 2 m vorticity (Apr 14, 2019 12Z) (f) 4-day bkwd. FTLE map at 4 m

Fig. 6: Dynamical flow structures in the Alboran Sea: MSEAS flow map, FTLE, and vorticity forecast products for April 10–14, 2019 (4-day duration). (a,b) 4-day forward x and y flow maps at 4 m; (c,f) 4-day forward and backward FTLEs show repelling and attracting regions in the Alboran Sea, respectively; (d–e) 2 m scaled vorticity snapshots at 12Z on April 12 and 14.

Program of the National Academies of Sciences, Engineering, and Medicine under award number 2000013149.

REFERENCES

[1] R. M. Samelson and S. Wiggins, *Lagrangian transport in geophysical jets and waves: The dynamical systems approach*. Springer Science & Business Media, 2006, vol. 31.

[2] A. Bennett, *Lagrangian fluid dynamics*. Cambridge University Press, 2006.

[3] A. Griffa, A. Kirwan Jr, A. J. Mariano, T. Özgökmen, and H. T. Rossby, *Lagrangian analysis and prediction of coastal and ocean dynamics*. Cambridge Univ. Press, 2007.

[4] P. Holmes, J. L. Lumley, G. Berkooz, and C. W. Rowley, *Turbulence, coherent structures, dynamical systems and symmetry*. Cambridge Univ. Press, 2012.

[5] S. V. Prants, "Chaotic Lagrangian transport and mixing in the ocean," *Eur. Phys. J. Special Topics*, vol. 223, no. 13, pp. 2723–2743, 2014.

[6] G. Haller, "Lagrangian coherent structures," *Annu. Rev. Fluid Mech.*, vol. 47, pp. 137–162, 2015.

[7] S. V. Prants, M. Y. Uleysky, and M. V. Budyansky, *Lagrangian oceanography: large-scale transport and mixing in the ocean*. Springer, 2017.

[8] E. van Sebille, S. M. Griffies, R. Abernathey, T. P. Adams, P. Berloff, A. Biastoch, B. Blanke, E. P. Chassignet, Y. Cheng, C. J. Cotter *et al.*, "Lagrangian ocean analysis: fundamentals and practices," *Ocean Model.*, 2017.

[9] G. A. Jacobs, H. S. Huntley, A. Kirwan Jr, B. L. Lipphardt Jr, T. Campbell, T. Smith, K. Edwards, and B. Bartels, "Ocean processes underlying surface clustering," *J. Geophys. Res. Oceans*, vol. 121, no. 1, pp. 180–197, 2016.

[10] P. F. J. Lermusiaux and F. Lekien, "Dynamics and Lagrangian coherent structures in the ocean and their uncertainty," in *Extended Abstract in report of the Dynamical System Methods in Fluid Dynamics Oberwolfach Workshop*, J. E. Marsden and J. Scheurle, Eds. Germany: Mathematisches Forschungsinstitut Oberwolfach, July 31st - August 6th 2005, p. 2.

[11] G. Haller, "An objective definition of a vortex," *J. Fluid Mech.*, vol. 525, pp. 1–26, 2005.

[12] G. Froyland, S. Lloyd, and N. Santitissadeekorn, "Coherent sets for nonautonomous dynamical systems," *Physica D*, vol. 239, no. 16, pp. 1527–1541, 2010.

[13] F. J. Beron-Vera, Y. Wang, M. J. Olascoaga, G. J. Goni, and G. Haller, "Objective detection of oceanic eddies and the agulhas leakage," *J. Phys. Oceanogr.*, vol. 43, no. 7, pp. 1426–1438, 2013.

[14] T. Peacock and G. Haller, "Lagrangian coherent structures: The hidden skeleton of fluid flows," *Physics today*, vol. 66, no. 2, pp. 41–47, 2013.

[15] A. Hadjighasem, M. Farazmand, D. Blazevski, G. Froyland, and G. Haller, "A critical comparison of lagrangian methods for coherent structure detection," *Chaos*, vol. 27, no. 5, p. 053104, 2017.

[16] F. Feppon and P. F. J. Lermusiaux, "Dynamically orthogonal numerical schemes for efficient stochastic advection and Lagrangian transport," *SIAM Rev.*, vol. 60, no. 3, pp. 595–625, 2018.

[17] C. S. Kulkarni and P. F. J. Lermusiaux, "Advection without compounding errors through flow map composition," *J. Comput. Phys.*, vol. 398, p. 108859, Dec. 2019.

[18] C. S. Kulkarni, "Prediction, analysis, and learning of advective transport in dynamic fluid flows," Ph.D. dissertation, Massachusetts Institute of Technology, Department of Mechanical Engineering and Center for Computational Science and Engineering, Cambridge, Massachusetts, Feb. 2021.

[19] C. S. Kulkarni and P. F. J. Lermusiaux, "Persistent Lagrangian material coherence in fluid and ocean flows using flow map composition," 2025, in preparation.

[20] F. Feppon and P. F. J. Lermusiaux, "Rigid sets and coherent sets in realistic ocean flows," 2025, in preparation.

[21] M. M. Doshi, C. S. Kulkarni, W. H. Ali, A. Gupta, P. F. J. Lermusiaux, P. Zhan, I. Hoteit, and O. Knio, "Flow maps and coherent sets for characterizing residence times and connectivity in lagoons and coral reefs: The case of the Red Sea," in *Oceans*. IEEE, Oct. 2019, pp. 1–8.

[22] P. F. J. Lermusiaux, M. Doshi, C. S. Kulkarni, A. Gupta, P. J. Haley, Jr., C. Mirabito, F. Trotta, S. J. Levang, G. R. Flierl, J. Marshall, T. Peacock, and C. Noble, "Plastic pollution in the coastal oceans: Characterization and modeling," in *Oceans*. IEEE, Oct. 2019, pp. 1–10.

Authorized licensed use limited to: MIT. Downloaded on December 03,2025 at 16:46:51 UTC from IEEE Xplore. Restrictions apply.

[23] MSEAS CALYPSO Ex., "CALYPSO real-time sea experiment 2019: Alboran Sea – March - April 2019," Apr. 2019, Accessed 2025-01-30. [Online]. Available: http://mseas.mit.edu/Sea_exercises/CALYPSO/2019/

[24] ——, "CALYPSO real-time Balearic Sea experiment 2022: Balearic Sea – February - June 2022," Jun. 2022. [Online]. Available: http://mseas.mit.edu/Sea_exercises/CALYPSO/2022/

[25] P. J. Haley, Jr. and P. F. J. Lermusiaux, "Multiscale two-way embedding schemes for free-surface primitive equations in the "Multidisciplinary Simulation, Estimation and Assimilation System"," *Ocean Dynam.*, vol. 60, no. 6, pp. 1497–1537, Dec. 2010.

[26] P. J. Haley, Jr., A. Agarwal, and P. F. J. Lermusiaux, "Optimizing velocities and transports for complex coastal regions and archipelagos," *Ocean Model.*, vol. 89, pp. 1–28, May 2015.

[27] P. J. Haley, Jr., C. Mirabito, M. Doshi, and P. F. J. Lermusiaux, "Ensemble forecasting for the Gulf of Mexico Loop Current region," in *Oceans*. Biloxi, MS: IEEE, Sep. 2023.

[28] G. You, T. Wong, and S. Leung, "Eulerian methods for visualizing continuous dynamical systems using Lyapunov exponents," *SIAM J. Sci. Comput.*, vol. 39, no. 2, pp. A415–A437, 2017.

[29] G. You and S. Leung, "Eulerian based interpolation schemes for flow map construction and line integral computation with applications to Lagrangian coherent structures extraction," *J. Sci. Comput.*, pp. 1–27, 2017.

[30] MSEAS (Multidisciplinary Simulation, Estimation, and Assimilation Systems) Group, "Software," Aug. 2011. [Online]. Available: http://mseas.mit.edu/software/

[31] P. F. J. Lermusiaux, C.-S. Chiu, G. G. Gawarkiewicz, P. Abbot, A. R. Robinson, R. N. Miller, P. J. Haley, Jr, W. G. Leslie, S. J. Majumdar, A. Pang, and F. Lekien, "Quantifying uncertainties in ocean predictions," *Oceanography*, vol. 19, no. 1, pp. 92–105, 2006.

[32] W. G. Leslie, A. R. Robinson, P. J. Haley, Jr, O. Logutov, P. A. Moreno, P. F. J. Lermusiaux, and E. Coelho, "Verification and training of real-time forecasting of multi-scale ocean dynamics for maritime rapid environmental assessment," *J. Marine Syst.*, vol. 69, no. 1, pp. 3–16, 2008.

[33] J. Xu, P. F. J. Lermusiaux, P. J. Haley Jr., W. G. Leslie, and O. G. Logutov, "Spatial and Temporal Variations in Acoustic propagation during the PLUSNet-07 Exercise in Dabob Bay," in *Proceedings of Meetings on Acoustics (POMA)*, vol. 4. Acoustical Society of America 155th Meeting, 2008, p. 11.

[34] P. J. Haley, Jr., P. F. J. Lermusiaux, A. R. Robinson, W. G. Leslie, O. Logoutov, G. Cossarini, X. S. Liang, P. Moreno, S. R. Ramp, J. D. Doyle, J. Bellingham, F. Chavez, and S. Johnston, "Forecasting and reanalysis in the Monterey Bay/California Current region for the Autonomous Ocean Sampling Network-II experiment," *Deep Sea Res. Part II*, vol. 56, no. 3–5, pp. 127–148, Feb. 2009.

[35] P. F. J. Lermusiaux, J. Xu, C.-F. Chen, S. Jan, L. Chiu, and Y.-J. Yang, "Coupled ocean–acoustic prediction of transmission loss in a continental shelfbreak region: Predictive skill, uncertainty quantification, and dynamical sensitivities," *IEEE J. Oceanic Eng.*, vol. 35, no. 4, pp. 895–916, Oct. 2010.

[36] A. Gangopadhyay, P. F. Lermusiaux, L. Rosenfeld, A. R. Robinson, L. Calado, H. S. Kim, W. G. Leslie, and P. J. Haley, Jr., "The California Current system: A multiscale overview and the development of a feature-oriented regional modeling system (FORMS)," *Dynam. Atmos. Oceans*, vol. 52, no. 1–2, pp. 131–169, Sep. 2011, Special issue of Dynamics of Atmospheres and Oceans in honor of Prof. A. R. Robinson.

[37] S. R. Ramp, P. F. J. Lermusiaux, I. Shulman, Y. Chao, R. E. Wolf, and F. L. Bahr, "Oceanographic and atmospheric conditions on the continental shelf north of the Monterey Bay during August 2006," *Dynam. Atmos. Oceans*, vol. 52, no. 1–2, pp. 192–223, Sep. 2011, Special issue of Dynamics of Atmospheres and Oceans in honor of Prof. A. R. Robinson.

[38] P. F. J. Lermusiaux, P. J. Haley, W. G. Leslie, A. Agarwal, O. Logutov, and L. J. Burton, "Multiscale physical and biological dynamics in the Philippine Archipelago: Predictions and processes," *Oceanography*, vol. 24, no. 1, pp. 70–89, 2011.

[39] M. E. G. D. Colin, T. F. Duda, L. A. te Raa, T. van Zon, P. J. Haley, Jr., P. F. J. Lermusiaux, W. G. Leslie, C. Mirabito, F. P. A. Lam, A. E. Newhall, Y.-T. Lin, and J. F. Lynch, "Time-evolving acoustic propagation modeling in a complex ocean environment," in *OCEANS - Bergen, 2013*, 2013, pp. 1–9.

[40] S. M. Kelly and P. F. J. Lermusiaux, "Internal-tide interactions with Gulf Stream and Middle Atlantic Bight shelfbreak front," *J. Geophys. Res. Oceans*, vol. 121, pp. 6271–6294, 2016.

[41] D. N. Subramani and P. F. J. Lermusiaux, "Energy-optimal path planning by stochastic dynamically orthogonal level-set optimization," *Ocean Modeling*, vol. 100, pp. 57–77, 2016.

[42] D. N. Subramani, P. F. J. Lermusiaux, P. J. Haley, Jr., C. Mirabito, S. Jana, C. S. Kulkarni, A. Girard, D. Wickman, J. Edwards, and J. Smith, "Time-optimal path planning: Real-time sea exercises," in *Oceans*, Aberdeen, Jun. 2017.

[43] P. F. J. Lermusiaux, D. N. Subramani, J. Lin, C. S. Kulkarni, A. Gupta, A. Dutt, T. Lolla, P. J. Haley, Jr., W. H. Ali, C. Mirabito, and S. Jana, "A future for intelligent autonomous ocean observing systems," *J. Mar. Res.*, vol. 75, no. 6, pp. 765–813, Nov. 2017, the Sea. Volume 17, The Science of Ocean Prediction, Part 2.

[44] C. S. Kulkarni, P. J. Haley, Jr., P. F. J. Lermusiaux, A. Dutt, A. Gupta, C. Mirabito, D. N. Subramani, S. Jana, W. H. Ali, T. Peacock, C. M. Royo, A. Rzeznik, and R. Supekar, "Real-time sediment plume modeling in the Southern California Bight," in *Oceans 2018*. Charleston, SC: IEEE, Oct. 2018.

[45] A. Gupta, P. J. Haley, D. N. Subramani, and P. F. J. Lermusiaux, "Fish modeling and Bayesian learning for the Lakshadweep Islands," in *Oceans*. IEEE, Oct. 2019, pp. 1–10.

[46] T. M. S. Johnston, M. C. Schönau, T. Paluszkiewicz, J. A. MacKinnon, B. K. Arbic, P. L. Colin, M. H. Alford, M. Andres, L. Centurioni, H. C. Graber, K. R. Helfrich, V. Hormann, P. F. J. Lermusiaux, R. C. Musgrave, B. S. Powell, B. Qiu, D. L. Rudnick, H. L. Simmons, L. St. Laurent, E. J. Terrill, D. S. Trossman, G. Voet, H. W. Wijesekera, and K. L. Zeiden, "Flow Encountering Abrupt Topography (FLEAT): A multiscale observational and modeling program to understand how topography affects flows in the western North Pacific," *Oceanog.*, vol. 32, no. 4, pp. 10–21, Dec. 2019.

[47] T. M. S. Johnston, J. A. MacKinnon, P. L. Colin, P. J. Haley, Jr., P. F. J. Lermusiaux, A. J. Lucas, M. A. Merrifield, S. T. Merrifield, C. Mirabito, J. D. Nash, C. Y. Ou, M. Siegelman, E. J. Terrill, and A. F. Waterhouse, "Energy and momentum lost to wake eddies and lee waves generated by the North Equatorial Current and tidal flows at Peleliu, Palau," *Oceanog.*, vol. 32, no. 4, pp. 110–125, Dec. 2019.

[48] Y. Pan, P. J. Haley, Jr., and P. F. J. Lermusiaux, "Interactions of internal tides with a heterogeneous and rotational ocean," *J. Fluid Mech.*, vol. 920, p. A18, Aug. 2021.

[49] M. Garcia-Jove, B. Mourre, N. D. Zarokanellos, P. F. J. Lermusiaux, D. L. Rudnick, and J. Tintoré, "Frontal dynamics in the Alboran Sea: 2. Processes for vertical velocities development," *J. Geophys. Res. Oceans*, vol. 127, no. 3, p. e2021JC017428, Mar. 2022.

[50] H. M. Aravind, V. Verma, S. Sarkar, M. A. Freilich, A. Mahadevan, P. J. Haley, Jr., P. F. J. Lermusiaux, and M. R. Allshouse, "Lagrangian surface signatures reveal upper-ocean vertical displacement conduits near oceanic density fronts," *Ocean Model.*, vol. 181, p. 102136, Feb. 2023.

[51] E. Rajagopal, A. N. S. Babu, T. Ryu, P. J. Haley, Jr.,

Authorized licensed use limited to: MIT. Downloaded on December 03,2025 at 16:46:51 UTC from IEEE Xplore. Restrictions apply.

C. Mirabito, and P. F. J. Lermusiaux, "Evaluation of deep neural operator models toward ocean forecasting," in *Oceans*. Biloxi, MS: IEEE, Sep. 2023.

[52] P. F. J. Lermusiaux, P. J. Haley, Jr., C. Mirabito, E. M. Mule, S. F. DiMarco, A. Dancer, X. Ge, A. H. Knap, Y. Liu, S. Mahmud, U. C. Nwankwo, S. Glenn, T. N. Miles, D. Aragon, K. Coleman, M. Smith, M. Leber, R. Ramos, J. Storie, G. Stuart, J. Marble, P. Barros, E. P. Chassignet, A. Bower, H. H. Furey, B. Jaimes de la Cruz, L. K. Shay, M. Tenreiro, E. Pallàs Sanz, J. Sheinbaum, P. Pérez Brunius, D. Wilson, J. van Smirren, R. Monreal Jiménez, D. A. Salas de León, V. K. Contreras Tereza, M. Feldman, and M. Khadka, "Real-time ocean probabilistic forecasts, reachability analysis, and adaptive sampling in the Gulf of Mexico," in *Oceans*. Halifax: IEEE, Sep. 2024, pp. 1–10.

[53] M. M. N. Robin, P. J. Haley, Jr., C. Mirabito, and P. F. J. Lermusiaux, "Dynamically-orthogonal parabolic equations for probabilistic ocean acoustics in the New England Seamounts," in *Oceans*. Halifax: IEEE, Sep. 2024, pp. 1–8.

[54] A. Agarwal and P. F. J. Lermusiaux, "Statistical field estimation for complex coastal regions and archipelagos," *Ocean Model.*, vol. 40, no. 2, pp. 164–189, 2011.

[55] O. G. Logutov and P. F. J. Lermusiaux, "Inverse barotropic tidal estimation for regional ocean applications," *Ocean Model.*, vol. 25, no. 1–2, pp. 17–34, 2008.

[56] P. F. J. Lermusiaux, "Evolving the subspace of the three-dimensional multiscale ocean variability: Massachusetts Bay," *J. Marine Syst.*, vol. 29, no. 1, pp. 385–422, 2001.

[57] P. F. J. Lermusiaux, "Uncertainty estimation and prediction for interdisciplinary ocean dynamics," *J. Comput. Phys.*, vol. 217, no. 1, pp. 176–199, 2006.

[58] P. F. J. Lermusiaux and A. R. Robinson, "Data assimilation via Error Subspace Statistical Estimation, part I: Theory and schemes," *Mon. Weather Rev.*, vol. 127, no. 7, pp. 1385–1407, 1999.

[59] P. F. J. Lermusiaux, "Data assimilation via Error Subspace Statistical Estimation, part II: Mid-Atlantic Bight shelfbreak front simulations, and ESSE validation," *Mon. Weather Rev.*, vol. 127, no. 7, pp. 1408–1432, Jul. 1999.

[60] ——, "Estimation and study of mesoscale variability in the Strait of Sicily," *Dynam. Atmos. Oceans*, vol. 29, no. 2, pp. 255–303, 1999.

[61] P. F. J. Lermusiaux, "Adaptive modeling, adaptive data assimilation and adaptive sampling," *Physica D*, vol. 230, no. 1, pp. 172–196, 2007.

[62] F.-P. A. Lam, P. J. Haley, Jr., J. Janmaat, P. F. J. Lermusiaux, W. G. Leslie, M. W. Schouten, L. A. te Raa, and M. Rixen, "At-sea real-time coupled four-dimensional oceanographic and acoustic forecasts during Battlespace Preparation 2007," *J. Marine Syst.*, vol. 78, no. Supplement, pp. S306–S320, Nov. 2009.

[63] T. F. Duda, Y.-T. Lin, A. E. Newhall, K. R. Helfrich, J. F. Lynch, W. G. Zhang, P. F. J. Lermusiaux, and J. Wilkin, "Multiscale multiphysics data-informed modeling for three-dimensional ocean acoustic simulation and prediction," *J. Acoust. Soc. Am.*, vol. 146, no. 3, pp. 1996–2015, Sep. 2019.

[64] P. F. J. Lermusiaux, C. Mirabito, P. J. Haley, Jr., W. H. Ali, A. Gupta, S. Jana, E. Dorfman, A. Laferriere, A. Kofford, G. Shepard, M. Goldsmith, K. Heaney, E. Coelho, J. Boyle, J. Murray, L. Freitag, and A. Morozov, "Real-time probabilistic coupled ocean physics-acoustics forecasting and data assimilation for underwater GPS," in *Oceans*. IEEE, 2020, pp. 1–9.

[65] P. F. J. Lermusiaux, P. J. Haley, Jr., C. Mirabito, W. H. Ali, M. Bhabra, P. Abbot, C.-S. Chiu, and C. Emerson, "Multiresolution probabilistic ocean physics-acoustic modeling: Validation in the New Jersey continental shelf," in *Oceans*. IEEE, Oct. 2020, pp. 1–9.

[66] W. H. Ali, A. Charous, C. Mirabito, P. J. Haley, Jr., and P. F. J. Lermusiaux, "MSEAS-ParEq for ocean-acoustic modeling around the globe," in *Oceans*. Biloxi, MS: IEEE, Sep. 2023.

[67] Ş. T. Beşiktepe, P. F. J. Lermusiaux, and A. R. Robinson, "Coupled physical and biogeochemical data-driven simulations of Massachusetts Bay in late summer: Real-time and post-cruise data assimilation," *J. Marine Syst.*, vol. 40–41, pp. 171–212, 2003.

[68] G. Cossarini, P. F. J. Lermusiaux, and C. Solidoro, "Lagoon of Venice ecosystem: Seasonal dynamics and environmental guidance with uncertainty analyses and error subspace data assimilation," *J. Geophys. Res. Oceans*, vol. 114, no. C6, Jun. 2009.

[69] P. J. Haley, Jr., A. Gupta, C. Mirabito, and P. F. J. Lermusiaux, "Towards Bayesian ocean physical-biogeochemical-acidification prediction and learning systems for Massachusetts Bay," in *Oceans*. IEEE, Oct. 2020, pp. 1–9.

[70] A. Gupta and P. F. J. Lermusiaux, "Bayesian learning of coupled biogeochemical-physical models," *Prog. Oceanogr.*, vol. 216, p. 103050, May 2023.

[71] P. F. J. Lermusiaux, P. J. Haley, Jr, and N. K. Yilmaz, "Environmental prediction, path planning and adaptive sampling: Sensing and modeling for efficient ocean monitoring, management and pollution control," *Sea Technol.*, vol. 48, no. 9, pp. 35–38, 2007.

[72] D. Wang, P. F. J. Lermusiaux, P. J. Haley, Jr., D. Eickstedt, W. G. Leslie, and H. Schmidt, "Acoustically focused adaptive sampling and on-board routing for marine rapid environmental assessment," *J. Marine Syst.*, vol. 78, no. Supplement, pp. S393–S407, Nov. 2009.

[73] J. Coulin, P. J. Haley, Jr., S. Jana, C. S. Kulkarni, P. F. J. Lermusiaux, and T. Peacock, "Environmental ocean and plume modeling for deep sea mining in the Bismarck Sea," in *Oceans*, Anchorage, AK, Sep. 2017.

[74] C. Muñoz Royo, T. Peacock, M. H. Alford, J. A. Smith, A. Le Boyer, C. S. Kulkarni, P. F. J. Lermusiaux, P. J. Haley, Jr., C. Mirabito, D. Wang, E. E. Adams, R. Ouillon, A. Breugem, B. Decrop, T. Lanckriet, R. B. Supekar, A. J. Rzeznik, A. Gartman, and S.-J. Ju, "Extent of impact of deep-sea nodule mining midwater plumes is influenced by sediment loading, turbulence and thresholds," *Nature Communications Earth & Environment*, vol. 2, no. 148, pp. 1–16, Jul. 2021.

[75] M. Tieppo, E. Pereira, L. González Garcia, M. Rolim, E. Castanho, A. Matos, A. Silva, B. Ferreira, M. Pascoal, E. Almeida, F. Costa, F. Zabel, J. Faria, J. Azevedo, J. Alves, J. Moutinho, L. Gonçalves, M. Martins, N. Cruz, N. Abreu, P. Silva, R. Viegas, S. Jesus, T. Chen, T. Miranda, A. Papalia, D. Hart, J. Leonard, M. Haji, O. de Weck, P. Godart, and P. Lermusiaux, "Submarine cables as precursors of persistent systems for large scale oceans monitoring and autonomous underwater vehicles operation," in *Oceans 2022*. Hampton Roads, VA: IEEE, Oct. 2022, pp. 1–7.

[76] M. Rixen, P. F. J. Lermusiaux, and J. Osler, "Quantifying, predicting, and exploiting uncertainties in marine environments," *Ocean Dynam.*, vol. 62, no. 3, pp. 495–499, 2012.

[77] M. De Dominicis, S. Falchetti, F. Trotta, N. Pinardi, L. Giacomelli, E. Napolitano, L. Fazioli, R. Sorgente, P. J. Haley, Jr., P. F. J. Lermusiaux, F. Martins, and M. Cocco, "A relocatable ocean model in support of environmental emergencies," *Ocean Dynam.*, vol. 64, no. 5, pp. 667–688, 2014.

[78] J. P. Heuss, P. J. Haley, Jr., C. Mirabito, E. Coelho, M. C. Schönau, K. Heaney, and P. F. J. Lermusiaux, "Reduced order modeling for stochastic prediction onboard autonomous platforms at sea," in *Oceans*. IEEE, Oct. 2020, pp. 1–10.

[79] T. Ryu, J. P. Heuss, P. J. Haley, Jr., C. Mirabito, E. Coelho, P. Hursky, M. C. Schönau, K. Heaney, and P. F. J. Lermusiaux,

Authorized licensed use limited to: MIT. Downloaded on December 03,2025 at 16:46:51 UTC from IEEE Xplore. Restrictions apply.

"Adaptive stochastic reduced order modeling for autonomous ocean platforms," in *Oceans 2021*. IEEE, Sep. 2021, pp. 1–9.
[80] T. Ryu, W. H. Ali, P. J. Haley, Jr., C. Mirabito, A. Charous, and P. F. J. Lermusiaux, "Incremental low-rank dynamic mode decomposition model for efficient dynamic forecast dissemination and onboard forecasting," in *Oceans 2022*. Hampton Roads, VA: IEEE, Oct. 2022, pp. 1–8.
[81] T. Lolla, P. F. J. Lermusiaux, M. P. Ueckermann, and P. J. Haley, Jr., "Time-optimal path planning in dynamic flows using level set equations: Theory and schemes," *Ocean Dynam.*, vol. 64, no. 10, pp. 1373–1397, 2014.
[82] T. Lolla, P. J. Haley, Jr., and P. F. J. Lermusiaux, "Time-optimal path planning in dynamic flows using level set equations: Realistic applications," *Ocean Dynam.*, vol. 64, no. 10, pp. 1399–1417, 2014.
[83] P. F. J. Lermusiaux, T. Lolla, P. J. Haley, Jr., K. Yigit, M. P. Ueckermann, T. Sondergaard, and W. G. Leslie, "Science of autonomy: Time-optimal path planning and adaptive sampling for swarms of ocean vehicles," in *Springer Handbook of Ocean Engineering*, T. Curtin, Ed. Springer, 2016, ch. 21, pp. 481–498.
[84] D. N. Subramani, P. J. Haley, Jr., and P. F. J. Lermusiaux, "Energy-optimal path planning in the coastal ocean," *J. Geophys. Res. Oceans*, vol. 122, pp. 3981–4003, 2017.
[85] D. N. Subramani, Q. J. Wei, and P. F. J. Lermusiaux, "Stochastic time-optimal path-planning in uncertain, strong, and dynamic flows," *Comput. Meth. Appl. Mech. Engrg.*, vol. 333, pp. 218–237, 2018.
[86] D. N. Subramani and P. F. J. Lermusiaux, "Risk-optimal path planning in stochastic dynamic environments," *Comput. Meth. Appl. Mech. Engrg.*, vol. 353, pp. 391–415, Aug. 2019.
[87] C. S. Kulkarni and P. F. J. Lermusiaux, "Three-dimensional time-optimal path planning in the ocean," *Ocean Model.*, vol. 152, Aug. 2020.
[88] M. Doshi, M. Bhabra, M. Wiggert, C. J. Tomlin, and P. F. J. Lermusiaux, "Hamilton–Jacobi multi-time reachability," in *IEEE 61st CDC*, Cuncún, Dec. 2022, pp. 2443–2450.
[89] M. M. Doshi, M. S. Bhabra, and P. F. J. Lermusiaux, "Energy-time optimal path planning in dynamic flows: Theory and schemes," *Computer Methods in Applied Mechanics and Engineering*, vol. 405, p. 115865, Feb. 2023.
[90] B. Schnitzler, P. J. Haley, Jr., C. Mirabito, E. M. Mule, J.-M. Moschetta, D. Delahaye, A. Drouin, and P. F. J. Lermusiaux, "Hazard-time optimal path planning for collaborative air and sea drones," in *Oceans*. Halifax: IEEE, Sep. 2024, pp. 1–10.
[91] P. F. J. Lermusiaux, P. J. Haley, Jr., S. Jana, A. Gupta, C. S. Kulkarni, C. Mirabito, W. H. Ali, D. N. Subramani, A. Dutt, J. Lin, A. Shcherbina, C. Lee, and A. Gangopadhyay, "Optimal planning and sampling predictions for autonomous and Lagrangian platforms and sensors in the northern Arabian Sea," *Oceanog.*, vol. 30, no. 2, pp. 172–185, Jun. 2017.
[92] K. D. Heaney, G. Gawarkiewicz, T. F. Duda, and P. F. J. Lermusiaux, "Nonlinear optimization of autonomous undersea vehicle sampling strategies for oceanographic data-assimilation," *J. Field Robot.*, vol. 24, no. 6, pp. 437–448, 2007.
[93] K. D. Heaney, P. F. J. Lermusiaux, T. F. Duda, and P. J. Haley, Jr., "Validation of genetic algorithm based optimal sampling for ocean data assimilation," *Ocean Dynam.*, vol. 66, pp. 1209–1229, 2016.
[94] C. Mirabito *et al.*, "Real-time optimal planning and adaptive sampling for multi-platform operations in the Gulf of Mexico," in *Oceans*. Chicago: IEEE, Sep. 2025, in press.
[95] MSEAS NESMA Ex., "New England Seamounts Experiment Acoustics (NESMA) 2024: New England Seamount Chain – July, 2024," Jul. 2024. [Online]. Available: http://mseas.mit.edu/Sea_exercises/NESMA/
[96] B. Tozer, D. T. Sandwell, W. H. F. Smith, C. Olson, J. R. Beale, and P. Wessel, "Global bathymetry and topography at 15 arc sec: SRTM15+," *Earth Space Sci.*, vol. 6, no. 10, pp. 1847–1864, Oct. 2019.
[97] NOAA National Centers for Environmental Information, "Coastal relief models (CRMs) [data set]," 2023, Accessed 2024-05-13. [Online]. Available: https://doi.org/10.25921/5ZN5-KN44
[98] T. J. McDougall and O. A. Krzysik, "Spiciness," *J. Mar. Res.*, vol. 73, no. 5, pp. 141–152, 2015.
[99] A. Silver, A. Gangopadhyay, G. Gawarkiewicz, E. N. S. Silva, and J. Clark, "Interannual and seasonal asymmetries in gulf stream ring formations from 1980 to 2019," *Sci. Rep.*, vol. 11, no. 1, p. 2207, 2021.
[100] A. Silver, A. Gangopadhyay, G. Gawarkiewicz, M. Andres, G. Flierl, and J. Clark, "Spatial variability of movement, structure, and formation of warm core rings in the northwest atlantic slope sea," *J. Geophys. Res. Oceans*, vol. 127, no. 8, p. e2022JC018737, 2022.
[101] MSEAS MASTR Ex., "MASTR Real-time Gulf of Mexico Sea Experiment 2024: Gulf of Mexico – February–April, 2024," Apr. 2024. [Online]. Available: http://mseas.mit.edu/Sea_exercises/GOFFISH/MASTR/
[102] M. Garcia-Jove, B. Mourre, N. Zarokanellos, P. F. J. Lermusiaux, P. J. Haley, Jr., C. Mirabito, D. L. Rudnick, and J. Tintoré, "Formation and evolution of a mesoscale density front and its associated submesoscale cyclonic eddies, and impact on subduction," *J. Geophys. Res. Oceans*, 2025, in preparation.
[103] M. Juza, B. Mourre, L. Renault, S. Gómara, K. Sebastián, S. Lora, J. P. Beltran, B. Frontera, B. Garau, C. Troupin, M. Torner, E. Heslop, B. Casas, R. Escudier, G. Vizoso, and J. Tintoré, "SOCIB operational ocean forecasting system and multi-platform validation in the western Mediterranean Sea," *J. Op. Oceanog.*, vol. 9, no. S1, pp. s155–s166, 2016.
[104] B. Mourre, E. Aguiar, M. Juza, J. Hernandez-Lasheras, E. Reyes, E. Heslop, R. Escudier, E. Cutolo, S. Ruiz, E. Mason, A. Pascual, and J. Tintore, "Assessment of high-resolution regional ocean prediction systems using multi-platform observations: Illustrations in the western Mediterranean Sea," in *New Frontiers in Operational Oceanography*. GODAE OceanView, Aug. 2018, ch. 24, pp. 663–694.
[105] W. H. Ali, M. H. Mirhi, A. Gupta, C. S. Kulkarni, C. Foucart, M. M. Doshi, D. N. Subramani, C. Mirabito, P. J. Haley, Jr., and P. F. J. Lermusiaux, "SeaVizKit: Interactive maps for ocean visualization," in *Oceans*. IEEE, Oct. 2019, pp. 1–10.
[106] Y. Gao, W. H. Ali, C. Foucart, C. Mirabito, P. J. Haley, Jr., and P. F. J. Lermusiaux, "3DSeaVizKit: An interactive spatiotemporal visualization toolkit for ocean data," *J. Atmos. Ocean. Tech.*, 2025, in preparation.
[107] H. S. Huntley, B. L. Lipphardt, Jr., G. Jacobs, and A. D. Kirwan, Jr., "Clusters, deformation, and dilation: Diagnostics for material accumulation regions," *J. Geophys. Res. Oceans*, vol. 120, no. 10, pp. 6622–6636, 2015.
[108] H. M. Aravind, T. M. Özgökmen, and M. R. Allshouse, "Lagrangian analysis of submesoscale flows from sparse data using Gaussian process regression for field reconstruction," *Ocean Model.*, vol. 193, p. 102458, 2025.
[109] M. Garcia-Jove, B. Mourre, N. Zarokanellos, P. Lermusiaux, D. Rudnick, J. Allen, and J. Tintoré, "Analysis of vertical velocities development through high-resolution simulation and glider observations in the Alboran Sea," in *EGU Gen. Assem.*, 2021, pp. EGU21–8945.
[110] N. Zarokanellos, D. Rudnick, M. Garcia-Jove, B. Mourre, S. Ruiz, A. Pascual, and J. Tintoré, "Frontal dynamics in the Alboran Sea: 1. coherent 3D pathways at the Almeria-Oran front using underwater glider observations," *J. Geophys. Res. Oceans*, vol. 127, no. 3, p. 2021JC017405, Mar. 2022.

Authorized licensed use limited to: MIT. Downloaded on December 03,2025 at 16:46:51 UTC from IEEE Xplore. Restrictions apply.